## Physics: Theory, Methodology and Practice

Editor Prof. Hakan Öztürk, Ph.D.

## Physics: Theory, Methodology, and Application

Prof. Hakan Öztürk, Ph.D.

#### **Publisher**

Platanus Publishing®

#### **Editor in Chief**

Prof. Hakan Öztürk, Ph.D.

#### **Cover & Interior Design**

Platanus Publishing®

#### The First Edition

October, 2025

#### **ISBN**

978-625-6454-50-7

#### **©copyright**

All rights reserved. No part of this publication may be reproduced or transmitted in any form or by any means, electronic or mechanical, including photocopy, or any information storage or retrieval system, without permission from the publisher.

#### **Platanus Publishing®**

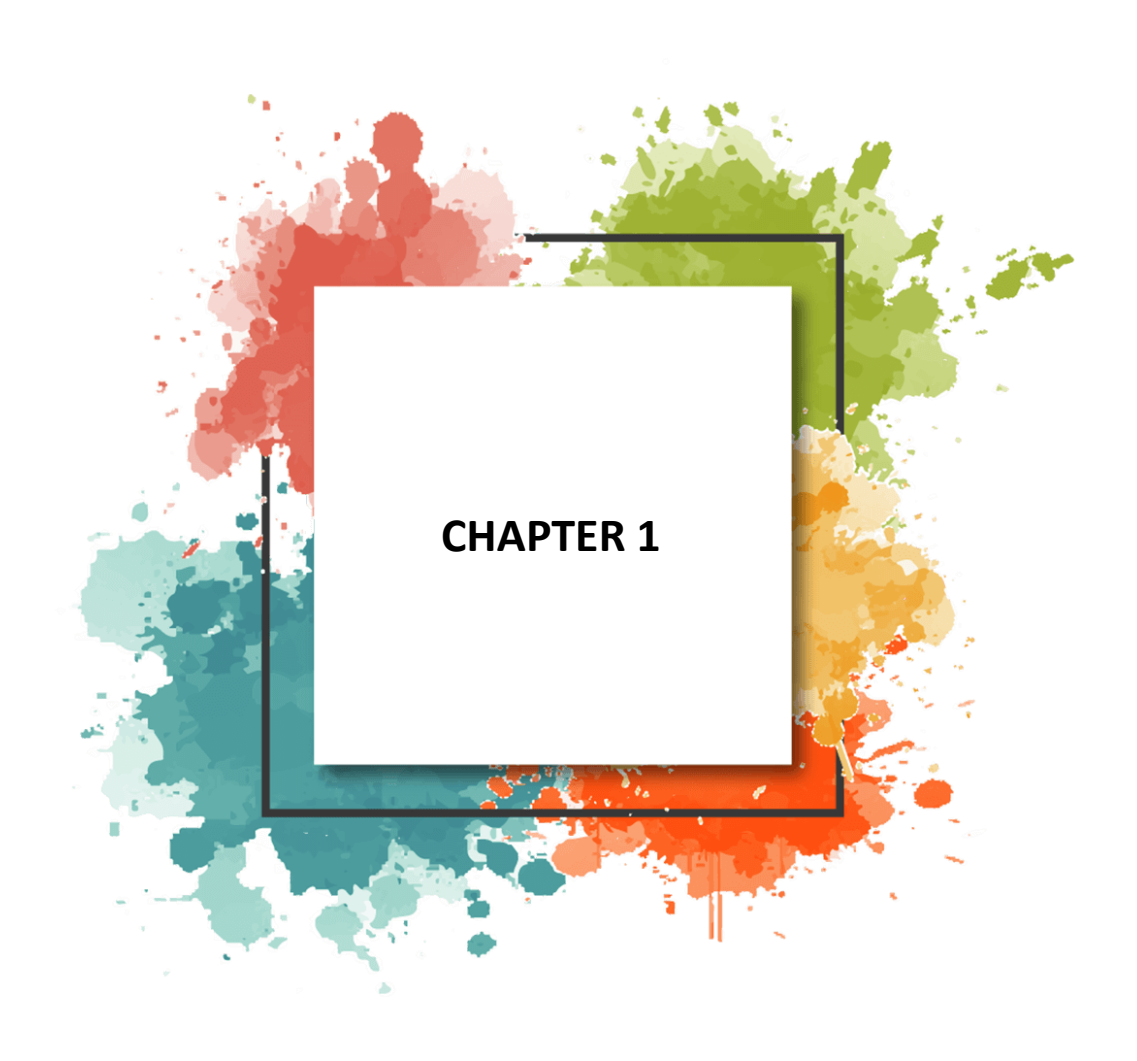
**Address:** Natoyolu Cad. Fahri Korutürk Mah. 157/B, 06480, Mamak, Ankara, Turkey.

**Phone:** +90 312 390 1 118 **web:** www.platanuspublishing.com **e-mail:** platanuskitap@gmail.com



### **CONTENTS**

Cŀ	APTER 1 5
	Computational Design of Quantum Materials: Dft Approaches for Qubit Realization  Aslı Öztürk Kiraz
Cŀ	1APTER 2 21
	Comparative Study of Photocatalytic Degradation of Various Organic Dyes Using Undoped and Gadolinium-Doped Zinc Oxide (Gd:ZnO) Nanoparticles ipek Balnan



### Computational Design of Quantum Materials: Dft Approaches for Qubit Realization

Aslı Öztürk Kiraz<sup>1</sup>

#### 1. Introduction

Quantum computing is emerging as one of the most transformative technologies of the 21st century, offering the promise of exponential speedups across various fields, including cryptography, optimization, machine learning, and drug discovery. At the heart of every quantum computing platform is the qubit, the quantum counterpart to the classical bit. Unlike classical bits, qubits can exist in superposition states and exhibit entanglement, leading to a fundamentally different computing paradigm. Numerous types of qubits have been investigated, such as spin-based qubits utilizing quantum dots (Loss & DiVincenzo, 1998), superconducting transmon qubits (Koch et al., 2007), photonics-based platforms (O'Brien, Furusawa, & Vučković, 2009), and topological states based on Majorana fermions (Alicea, 2012). Each type of qubit imposes specific requirements on the materials used, including long coherence times, resistance to noise, and tunability of quantum states. In this context, computational materials science plays a vital role. Density Functional Theory (DFT) serves as a powerful tool for predicting the structural, electronic, and magnetic properties of candidate materials prior to their synthesis. Compared to experimental approaches, computational design is not only quicker and more cost-effective but also allows for a systematic exploration of extensive chemical and structural spaces. Nonetheless, it does face limitations, such as the inability to directly model decoherence mechanisms, approximations in exchangecorrelation functionals, and the challenge of bridging the gap from atomic-level properties to device performance.

#### 2. Condensed Functional Theory in Quantum Materials

#### 2.1 Fundamentals of DFT and the Hohenberg-Kohn Theorems

DFT is the most prevalent ab initio method for predicting the ground-state properties of quantum materials. The Hohenberg–Kohn theorems establish that the ground-state energy of a many-particle electron system is uniquely defined by the electron density  $(\rho(r))$  (Hohenberg & Kohn, 1964). The Kohn–Sham

<sup>&</sup>lt;sup>1</sup> Assoc. Prof. Dr., Department of Physics, Faculty of Science, Pamukkale University ORCID: 0000- 0001- 9837-0779

formulation reformulates the many-body Schrödinger equation into a computationally self-consistent single-particle equation (Kohn & Sham, 1965).

#### 2.2 Exchange Correlation Functionals

The effectiveness of DFT is largely contingent upon the definition of the exchange-correlation (XC) energy. The primary approaches include:

- Local Density Approximation (LDA): This method is well-suited for homogeneous electron gases, yet it generally underestimates band gaps (Perdew & Zunger, 1981).
- Generalized Gradient Approximation (GGA): This approach is commonly employed for evaluating structural properties and energies, with the Perdew-Burke-Ernzerhof (PBE) functional being especially popular (Perdew, Burke, & Ernzerhof, 1996).
- Hybrid Functionals: These functionals enhance band gap predictions by incorporating a certain proportion of exact exchange (Heyd, Scuseria, & Ernzerhof, 2003; Krukau, Vydrov, Izmaylov, & Scuseria, 2006).

Accurate predictions of band gaps, spin polarization, and magnetic anisotropy are essential for quantum materials. Consequently, the choice of functional can greatly influence the outcomes.

#### 2.3 Spin-Orbit Coupling and Magnetism

Spin-orbit coupling (SOC) is a crucial factor in materials such as topological insulators and spin-based qubits. It enables significant phenomena like band inversion, spin separation, and the formation of protected surface states. By integrating SOC into DFT, researchers can effectively model important qubit phenomena, including the Rashba effect, quantum spin Hall states, and Majorana modes (Koelling & Harmon, 1977).

#### 2.4 Beyond the Ground State: TD-DFT and Many-Body Corrections

Standard DFT primarily focuses on ground-state properties. Time-Dependent DFT (TD-DFT), however, facilitates the examination of excited-state dynamics, which is vital for the analysis of photonic qubits and decoherence processes (Runge & Gross, 1984). For more accurate predictions, many-body perturbation theory is utilized:

• GW Approximation (Green's function (G) + screened Coulomb interaction (W)): This technique enhances band gap estimates by correcting quasiparticle energies (Hedin, 1965).

• Bethe-Salpeter Equation (BSE): This method considers excitonic effects (Onida, Reining, & Rubio, 2002).

These approaches are essential for the design of materials where electronic excitations and shielding processes significantly influence qubit performance.

#### 3. Target Properties for Qubit Realization

#### 3.1 Coherence Time and Decoherence Mechanisms

A key challenge in qubit design is the preservation of quantum coherence. Qubit states engage with their environment, which results in decoherence over time and ultimately leads to the loss of quantum information. Coherence times, designated as T<sub>1</sub> and T<sub>2</sub>, are frequently constrained by factors such as phonon scattering, spin–orbit interactions, and charge fluctuations (Khaetskii, Loss, & Glazman, 2002; Ithier et al., 2005; Martinis et al., 2005). Furthermore, 1/f noise plays a significant role in limiting the performance of quantum information processing within solid-state systems (Paladino, Galperin, Falci, & Altshuler, 2014).

DFT does not directly calculate coherence times, but it provides essential parameters that influence them:

- Phonon Dispersion Relations (utilizing Density Functional Perturbation Theory - DFPT): These illustrate the interactions between qubits and lattice vibrations.
- Defect Energies and Charge States: These parameters help identify potential sources of noise within the system.
- Spin-Orbit Coupling (SOC) and Magnetic Anisotropy: These factors play a crucial role in determining the pathways for spin relaxation.

When integrated with detailed models of quantum systems, these parameters significantly contribute to the prediction of decoherence processes.

#### 3.2 Spin Polarization and Magnetic Anisotropy

The controllability of spin order is crucial for the functionality of spin-based qubits. High spin polarization and robust magnetic anisotropy are essential attributes that facilitate long-lived spin states, allowing for selective control using external fields.

• Spin polarization is directly assessed from the electronic density of states (DOS) derived from spin-polarized DFT calculations.

Magnetic anisotropy energy (MAE), typically calculated in conjunction with spin-orbit coupling (SOC), serves to stabilize qubit states against thermal fluctuations

• Orbital contributions play a particularly important role in transition metals and rare earth compounds.

As a result, design principles are oriented toward ensuring that spin states are both localized (which minimizes decoherence) and tunable (which is vital for gate operations).

#### 3.3 Band Topology and Surface States

Topological quantum materials, including Bi<sub>2</sub>Se<sub>3</sub> and Sb<sub>2</sub>Te<sub>3</sub>, serve as effective platforms for qubits, leveraging protected edge and surface states. These states exhibit resilience to backscattering, which positions them as a promising foundation for topological qubits.

DFT calculations that incorporate Spin-Orbit Coupling (SOC) facilitate the analysis of band inversion and the determination of the  $Z_2$  topological invariants. Furthermore, topological indicators such as Berry curvature and Chern numbers can be evaluated using models based on Wannier functions obtained from DFT (Xiao, Chang, & Niu, 2010). These findings are essential for the exploration of Majorana-bound states and for a deeper understanding of the quantum spin Hall effect.

#### 3.4 Charge Noise, Dielectric Response, and Structural Stability

In superconducting and solid-state qubits, charge noise—caused by defects, bond breaks, or fluctuations in the electric field—poses a significant source of decoherence. DFT provides valuable opportunities for investigating these effects:

- Point defects and vacancies: By evaluating formation energies and charge transition levels, DFT can indicate the likelihood of introducing charge noise.
- Dielectric response: Dielectric constants calculated using linear response theory help determine the extent to which charge fluctuations are shielded.
- Mechanical and thermal stability: Structural optimization and phonon calculations can reveal metastable phases or dynamic instabilities.

Therefore, DFT is instrumental not only in suggesting new materials but also in identifying and eliminating unstable or noise-prone candidates.

#### 4. Material Examples Related to Qubits

#### 4.1 Two-Dimensional (2D) Materials: Graphene, MoS2, h-BN

Two-dimensional materials are garnering considerable attention in qubit research due to their high surface-to-volume ratios, layered structures, and tunable electronic band structures.

- Graphene: While pristine graphene features a zero band gap, DFT studies reveal that this band gap can be increased through edge modifications, strain treatments, or the creation of heterostructures. The phenomena of spin–valley physics, along with the quantum Hall and quantum spin Hall effects, present promising avenues for graphene-based qubits (Castro Neto et al., 2009).
- MoS<sub>2</sub> (Molybdenum Disulfide): Single-layer MoS<sub>2</sub> exhibits semiconductor properties with a direct band gap. DFT calculations that incorporate Spin-Orbit Coupling (SOC) suggest that it is a viable candidate for spin and valley qubits due to its strong spin-valley coupling (Xiao, Liu, Feng, Xu, & Yao, 2012).
- h-BN: Hexagonal boron nitride (h-BN) is particularly valuable as a dielectric layer or for defect-centered qubits (similar to NV centers), thanks to its high bandgap and chemically stable structure (Tran, Bray, Ford, Toth, & Aharonovich, 2016).

An additional advantage of two-dimensional materials is their capacity to stack through van der Waals interactions, enabling their use in multilayer qubit architectures.

#### 4.2 Topological Insulators: Bi<sub>2</sub>Se<sub>3</sub>, Sb<sub>2</sub>Te<sub>3</sub>

Topological insulators stand out in qubit applications due to the protected surface states that emerge as a result of band inversion.

- DFT + SOC calculations play a critical role in determining the  $Z_2$  topological invariants and spin separations in the band structures in these materials (Fu & Kane, 2007).
- Compounds such as Bi<sub>2</sub>Se<sub>3</sub> and Sb<sub>2</sub>Te<sub>3</sub> have been associated with topological superconductivity, which can host Majorana fermions (Zhang et al., 2009; Xia et al., 2009).
- The robustness of these surface states against backscattering provides a significant advantage for fault-tolerant topological qubits (Hasan & Kane, 2010; Qi & Zhang, 2011).

Therefore, topological insulators are among the most promising materials for fault-tolerant quantum computing.

#### 4.3 Superconductors: Cuprates, NbSe<sub>2</sub>

Superconductor-based qubits, such as transmon qubits, are among the most widely utilized architectures today.

- Cuprates: These materials exhibit high-temperature superconductivity, yet their complex correlation effects pose challenges for a complete description using Density Functional Theory (DFT). Nonetheless, their quantum carrier properties can be effectively analyzed using hybrid DFT + Dynamical Mean-Field Theory (DMFT) calculations.
- NbSe<sub>2</sub> (Niyobyum Diselenid): Notable for its layered structure, NbSe<sub>2</sub> plays a significant role in the research of 2D superconductivity. DFT-based phonon calculations have substantiated BCS-like coupling mechanisms and illuminated the contribution of electron-phonon interactions. Additionally, the Ising pairing phenomenon has been observed, particularly in atomically thin layers of NbSe<sub>2</sub> (Xi et al., 2016).

In the realm of superconductors, DFT offers valuable insights for enhancing the robustness of qubit architectures by examining phonon spectra, Fermi surface topology, and electron–phonon interactions.

#### 4.4 Van der Waals Heterostructures and Moiré Physics

Van der Waals (vdW) heterostructures are created by stacking various 2D materials in layered configurations. These structures demonstrate unique quantum phenomena through interface engineering and the formation of moiré patterns.

- Moiré superlattices give rise to flat bands with low energy, which can lead to quantum magnetic phases and correlated electron states (Bistritzer & MacDonald, 2011).
- DFT-based calculations are employed to predict bandgap engineering, spintronic properties, and dielectric screening effects within these heterostructures.
- Correlated insulators and superconductivity have been observed, particularly in magic-angle graphene systems, which present new opportunities for quantum simulation and qubit interaction (Cao et al., 2018a, 2018b).

These heterostructures exemplify the concept of "tuning qubit properties through material design" most effectively.

#### 5. DFT-Based Workflow for Qubit Material Design

#### 5.1 High-Throughput Screens and Databases

High-throughput DFT calculations are essential for identifying suitable candidates for quantum materials, in contrast to conducting calculations on individual materials. Key resources in this area include:

- Materials Project: This is one of the most comprehensive databases, offering electronic and structural properties for thousands of materials (Jain et al., 2013).
- AFLOW: A framework designed for high-throughput automated materials discovery (Curtarolo et al., 2012).
- OQMD: This database provides extensive thermodynamic and electronic data across a wide range of materials (Saal, Kirklin, Aykol, Meredig, & Wolverton, 2013).
- Automated computational frameworks such as AiiDA and Atomate facilitate the management of large-scale DFT scans (Pizzi, Cepellotti, Sabatini, Marzari, & Kozinsky, 2016).

These databases enable filtering based on critical parameters relevant for qubits, including band gap, magnetic moment, and topological indicators.

#### 5.2 Structural Optimization, Phonon Distribution, and Stability Analyses

High-throughput DFT calculations are crucial for identifying suitable candidates for quantum materials, as opposed to conducting calculations on individual materials. Key resources in this area include:

- Materials Project: This is one of the most comprehensive databases, offering electronic and structural properties for thousands of materials (Jain et al., 2013).
- AFLOW: A framework designed for high-throughput automated materials discovery (Curtarolo et al., 2012).
- OQMD: This database provides extensive thermodynamic and electronic data across a wide range of materials (Saal, Kirklin, Aykol, Meredig, & Wolverton, 2013).

• Automated computational frameworks such as AiiDA and Atomate facilitate the management of large-scale DFT scans (Pizzi, Cepellotti, Sabatini, Marzari, & Kozinsky, 2016).

These databases enable filtering based on critical parameters relevant for qubits, including band gap, magnetic moment, and topological indicators.

#### 5.3 Band Structures, Density States, and Fermi Level Tuning

The electronic structure of qubit materials plays a crucial role in their functionality.

- Band Structure and Density of States (BDS): These factors dictate whether a material exhibits conductive, semiconductive, or insulating properties.
- Fermi Level Engineering: This can be achieved through methods such as doping, strain application, or heterostructure design. DFT is employed to predict how these modifications will impact the band structure.
- Spin-Coupled Band Separations and Topological Surface States: These fundamental parameters are key to determining the properties of qubits.

#### 5.4 Spin Texture and Berry Curvature Analysis

An important aspect influencing qubit performance is the examination of topological quantities, such as spin texture and Berry curvature.

- Spin Texture: This refers to the distribution of spin orientations within the band structure, which is analyzed through DFT + SOC calculations.
- Berry Curvature and Chern Numbers: These concepts assess the topological stability of qubits. Various tools, including wannier90 software (Mostofi et al., 2008, 2014), WannierTools (Wu, Zhang, Song, Troyer, & Soluyanov, 2018), and WannierBerri (Tsirkin, 2021), are utilized for this analysis.

These evaluations are particularly crucial when studying topological insulators, Weyl semimetals, and Majorana-based qubits.

#### 6. Limitations and Future Directions

#### 6.1 Prediction of Coherence and Decoherence Mechanisms

While DFT effectively predicts the electronic structure, phonon spectra, and magnetic properties of materials, it falls short in directly calculating quantum coherence times  $(T_1, T_2)$ . Decoherence processes generally involve multi-scale mechanisms, ranging from atomistic to device-level interactions, including interactions with phonons, charge noise, spin-orbit induced relaxation, and

fluctuations in magnetic fields. Consequently, outputs from DFT must be integrated with theories of quantum open systems, such as Lindblad equations or master equation models.

#### 6.2 Functional Selection and Computational Challenges

The effectiveness of DFT is heavily influenced by the choice of exchange-correlation (XC) functional employed.

- Local Density Approximation (LDA) and Generalized Gradient Approximation (GGA) tend to underestimate band gaps.
- Hybrid functionals offer more precise results, though they come with increased computational demands.
- For systems with strong correlations, such as cuprates and rare earth materials, it is essential to use DFT+U or DFT+DMFT methods.

This highlights the need to strike a balance between accuracy and computational cost, particularly in the context of high-throughput screening.

#### 6.3 Machine Learning Integration

In recent years, machine learning (ML) methods have surfaced as valuable complements to DFT calculations. Models trained on DFT results sourced from materials databases can swiftly predict the properties of new compounds. ML is increasingly utilized to rectify errors in functional selection, efficiently explore vast chemical spaces, and forecast coherence-related parameters. The development of specialized datasets tailored for quantum materials could be transformative for this field.

#### 6.4 Multiscale Modeling: From Atomistic to Device Level

Qubit performance is influenced not only by atomic-level material properties but also by device architecture, contacts, and environmental noise. While DFT is well-suited for examining atomic-scale phenomena, it falls short in capturing device-level behavior. To address this gap, multiscale modeling is necessary, encompassing:

- Atomistic level: DFT and ab initio calculations
- Mesoscopic level: Tight-binding and Hubbard models
- Macroscopic level: Circuit models and quantum error correction algorithms

In this context, defining band topology through metrics such as  $Z_2$  invariants (Kane & Mele, 2005) and incorporating the concept of Berry phases into

multiscale analyses (Xiao, Chang, & Niu, 2010) provide essential insights that bridge the divide between material design and practical quantum hardware implementation.

#### 7. Conclusion

Quantum computing has swiftly emerged as a transformative paradigm, with qubits serving as its essential building blocks. The realization of robust qubits fundamentally hinges on the discovery and design of novel quantum materials that can sustain coherence, exhibit tunable quantum states, and endure environmental perturbations. DFT has established itself as an indispensable tool in this endeavor, providing predictive insights into the structural, electronic, magnetic, and topological properties of candidate materials before they are synthesized. This chapter has underscored the crucial role of DFT in guiding the design of qubit materials, covering foundational topics such as exchangecorrelation functionals and spin-orbit coupling, as well as advanced frameworks like time-dependent DFT and many-body perturbation methods (GW, BSE). Case studies on two-dimensional semiconductors (e.g., MoS2, h-BN), topological insulators (Bi<sub>2</sub>Se<sub>3</sub>, Sb<sub>2</sub>Te<sub>3</sub>), and superconductors (NbSe<sub>2</sub>, cuprates) have illustrated the diverse material platforms available for qubit realization. Furthermore, high-throughput databases and automated workflows have facilitated large-scale material screening, while modern tools for spin texture and Berry curvature analysis have enriched our understanding of topological stability. Despite these advances, challenges persist. DFT alone cannot directly predict decoherence times, nor can it fully capture multi-scale device-level dynamics. Limitations in functional accuracy, the high cost of hybrid methods, and the complexities associated with strongly correlated systems complementary approaches such as DFT+U, DFT+DMFT, and the integration with machine learning models. Moreover, multiscale modeling frameworks that connect atomistic calculations with mesoscopic and macroscopic device models are essential for bridging the gap between theory and practical quantum hardware. Looking ahead, the synergy between DFT, advanced many-body techniques, high-throughput screening, and machine learning holds great promise for accelerating the discovery of next-generation quantum materials. By developing systematic frameworks that link fundamental material properties with devicelevel performance, computational design can play a pivotal role in overcoming current limitations and enabling scalable, fault-tolerant quantum computing.

#### References

- Alicea, J. (2012). New directions in the pursuit of Majorana fermions in solid state systems. *Reports on Progress in Physics*, 75(7), 076501. doi:10.1088/0034-4885/75/7/076501
- Baroni, S., de Gironcoli, S., Dal Corso, A., & Giannozzi, P. (2001). Phonons and related crystal properties from density-functional perturbation theory. *Reviews of Modern Physics*, 73(2), 515–562. doi:10.1103/RevModPhys.73.515
- Bistritzer, R., & MacDonald, A. H. (2011). Moiré bands in twisted double-layer graphene. *Proceedings of the National Academy of Sciences, 108*(30), 12233–12237. doi:10.1073/pnas.1108174108
- Cao, Y., Fatemi, V., Fang, S., Watanabe, K., Taniguchi, T., Kaxiras, E., & Jarillo-Herrero, P. (2018a). Correlated insulator behaviour at half-filling in magicangle graphene superlattices. *Nature*, 556(7699), 80–84. doi:10.1038/nature26154
- Cao, Y., Fatemi, V., Fang, S., Watanabe, K., Taniguchi, T., Kaxiras, E., & Jarillo-Herrero, P. (2018b). Unconventional superconductivity in magic-angle graphene superlattices. *Nature*, 556(7699), 43–50. doi:10.1038/nature26160
- Castro Neto, A. H., Guinea, F., Peres, N. M. R., Novoselov, K. S., & Geim, A. K. (2009). The electronic properties of graphene. *Reviews of Modern Physics*, 81(1), 109–162. doi:10.1103/RevModPhys.81.109
- Curtarolo, S., Setyawan, W., Hart, G. L. W., Jahnatek, M., Chepulskii, R. V., Taylor, R. H., Levy, O. (2012). AFLOW: An automatic framework for high-throughput materials discovery. *Computational Materials Science*, 58, 218–226. doi:10.1016/j.commatsci.2012.02.005
- Fu, L., & Kane, C. L. (2007). Topological insulators with inversion symmetry. *Physical Review B*, 76(4), 045302. doi:10.1103/PhysRevB.76.045302
- Hasan, M. Z., & Kane, C. L. (2010). Colloquium: Topological insulators. *Reviews of Modern Physics*, 82(4), 3045–3067. doi:10.1103/RevModPhys.82.3045
- Hedin, L. (1965). New method for calculating the one-particle Green's function with application to the electron-gas problem. *Physical Review, 139*(3A), A796–A823. doi:10.1103/PhysRev.139.A796
- Heyd, J., Scuseria, G. E., & Ernzerhof, M. (2003). Hybrid functionals based on a screened Coulomb potential. *Journal of Chemical Physics*, 118(18), 8207– 8215. doi:10.1063/1.1564060
- Hohenberg, P., & Kohn, W. (1964). Inhomogeneous electron gas. *Physical Review,* 136(3B), B864–B871. doi:10.1103/PhysRev.136.B864

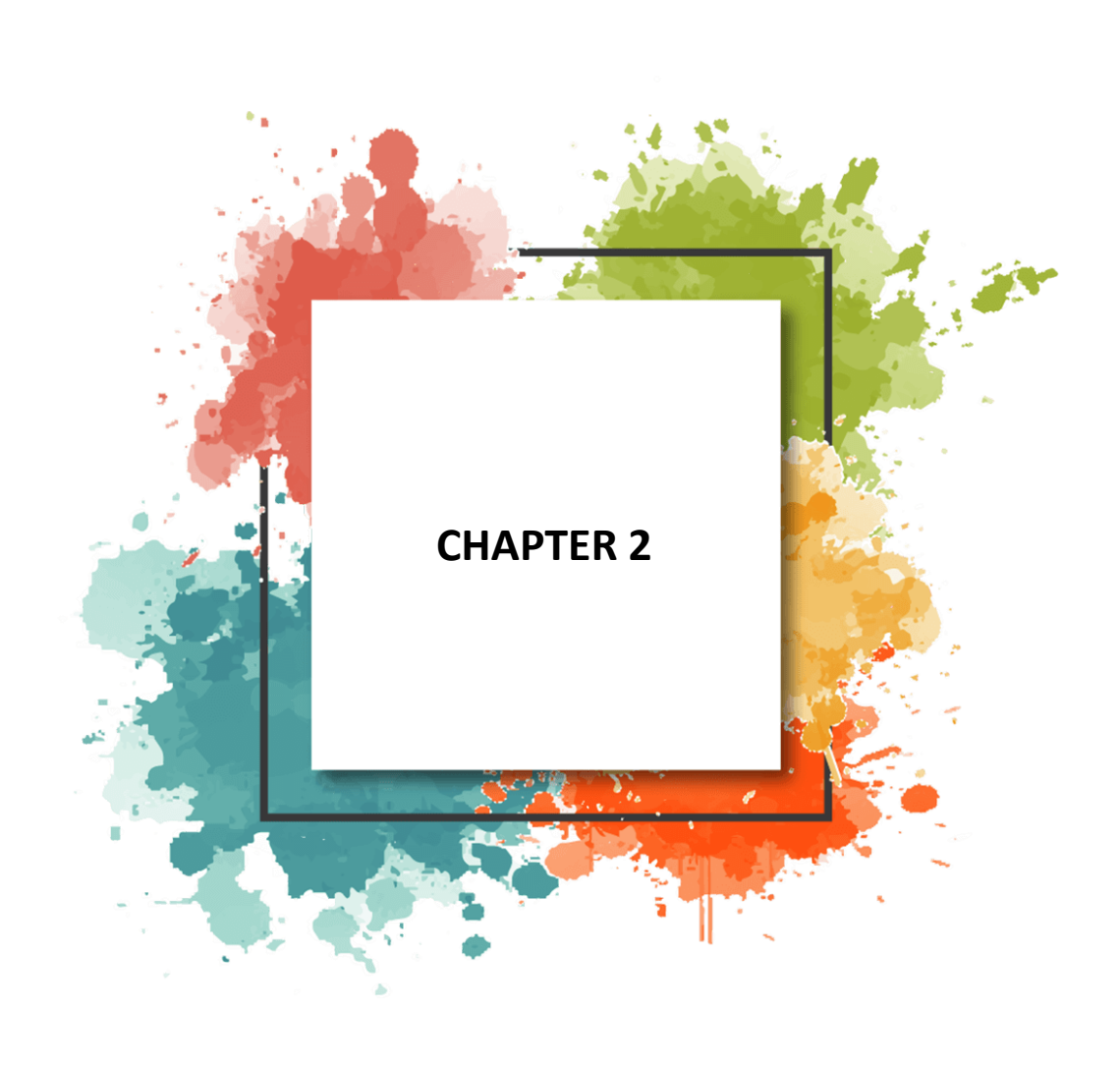
- Ithier, G., Collin, E., Joyez, P., Meeson, P. J., Vion, D., Esteve, D., Glattli, D. C. (2005). Decoherence in a superconducting quantum bit circuit. *Physical Review B*, 72(13), 134519. doi:10.1103/PhysRevB.72.134519
- Jain, A., Ong, S. P., Hautier, G., Chen, W., Richards, W. D., Dacek, S., Ceder, G. (2013). Commentary: The Materials Project: A materials genome approach to accelerating materials innovation. APL Materials, 1(1), 011002. doi:10.1063/1.4812323
- Kane, C. L., & Mele, E. J. (2005). Z<sub>2</sub> topological order and the quantum spin Hall effect. *Physical Review Letters*, 95(14), 146802. doi:10.1103/PhysRevLett.95.146802
- Koch, J., Yu, T. M., Gambetta, J., Houck, A. A., Schuster, D. I., Majer, J., Schoelkopf,
  R. J. (2007). Charge-insensitive qubit design derived from the Cooper pair box (transmon). *Physical Review A*, 76(4), 042319. doi:10.1103/PhysRevA.76.042319
- Koelling, D. D., & Harmon, B. N. (1977). A technique for relativistic spin-polarized calculations. *Journal of Physics C: Solid State Physics*, 10(16), 3107–3114. doi:10.1088/0022-3719/10/16/019
- Kohn, W., & Sham, L. J. (1965). Self-consistent equations including exchange and correlation effects. *Physical Review*, 140(4A), A1133–A1138. doi:10.1103/PhysRev.140.A1133
- Khaetskii, A. V., Loss, D., & Glazman, L. (2002). Electron spin decoherence in quantum dots due to interaction with nuclei. *Physical Review Letters*, 88(18), 186802. doi:10.1103/PhysRevLett.88.186802
- Krukau, A. V., Vydrov, O. A., Izmaylov, A. F., & Scuseria, G. E. (2006). Influence of the exchange screening parameter on the performance of screened hybrid functionals. *Journal of Chemical Physics*, 125(22), 224106. doi:10.1063/1.2404663
- Loss, D., & DiVincenzo, D. P. (1998). Quantum computation with quantum dots. *Physical Review A*, *57*(1), 120–126. doi:10.1103/PhysRevA.57.120
- Mostofi, A. A., Yates, J. R., Lee, Y.-S., Souza, I., Vanderbilt, D., & Marzari, N. (2008). Wannier90: A tool for obtaining maximally-localised Wannier functions. *Computer Physics Communications*, 178(9), 685–699. doi:10.1016/j.cpc.2007.11.016
- Mostofi, A. A., Yates, J. R., Pizzi, G., Lee, Y.-S., Souza, I., Vanderbilt, D., ... Marzari, N. (2014). An updated version of wannier90: A tool for obtaining maximally-localised Wannier functions. *Computer Physics Communications*, 185(8), 2309–2310. doi:10.1016/j.cpc.2014.05.003

- Martinis, J. M., Cooper, K. B., McDermott, R., Steffen, M., Ansmann, M., Osborn, K. D., Clarke, J. (2005). Decoherence in Josephson qubits from dielectric loss. *Physical Review Letters*, 95(21), 210503. doi:10.1103/PhysRevLett.95.210503
- O'Brien, J. L., Furusawa, A., & Vučković, J. (2009). Photonic quantum technologies. *Nature Photonics*, 3(12), 687–695. doi:10.1038/nphoton.2009.229
- Onida, G., Reining, L., & Rubio, A. (2002). Electronic excitations: Density-functional versus many-body Green's-function approaches. *Reviews of Modern Physics*, 74(2), 601–659. doi:10.1103/RevModPhys.74.601
- Paladino, E., Galperin, Y. M., Falci, G., & Altshuler, B. L. (2014). 1/f noise: Implications for solid-state quantum information. *Reviews of Modern Physics*, 86(2), 361–418. doi:10.1103/RevModPhys.86.361
- Perdew, J. P., & Zunger, A. (1981). Self-interaction correction to density-functional approximations for many-electron systems. *Physical Review B*, 23(10), 5048–5079. doi:10.1103/PhysRevB.23.5048
- Perdew, J. P., Burke, K., & Ernzerhof, M. (1996). Generalized gradient approximation made simple. *Physical Review Letters*, 77(18), 3865–3868. doi:10.1103/PhysRevLett.77.3865
- Pizzi, G., Cepellotti, A., Sabatini, R., Marzari, N., & Kozinsky, B. (2016). AiiDA: automated interactive infrastructure and database for computational science. *Computational Materials Science*, 111, 218–230. doi:10.1016/j.commatsci.2015.09.013
- Qi, X.-L., & Zhang, S.-C. (2011). Topological insulators and superconductors.

  \*Reviews of Modern Physics, 83(4), 1057–1110.

  doi:10.1103/RevModPhys.83.1057
- Runge, E., & Gross, E. K. U. (1984). Density-functional theory for time-dependent systems. *Physical Review Letters*, 52(12), 997–1000. doi:10.1103/PhysRevLett.52.997
- Saal, J. E., Kirklin, S., Aykol, M., Meredig, B., & Wolverton, C. (2013). Materials design and discovery with high-throughput density functional theory: The Open Quantum Materials Database (OQMD). *JOM*, 65(11), 1501–1509. doi:10.1007/s11837-013-0755-4
- Togo, A., & Tanaka, I. (2015). First principles phonon calculations in materials science. *Scripta Materialia*, 108, 1–5. doi:10.1016/j.scriptamat.2015.07.021

- Tran, T. T., Bray, K., Ford, M. J., Toth, M., & Aharonovich, I. (2016). Quantum emission from hexagonal boron nitride monolayers. *Nature Nanotechnology*, 11(1), 37–41. doi:10.1038/nnano.2015.242
- Tsirkin, S. S. (2021). High performance Wannier interpolation of Berry curvature and related quantities with WannierBerri code. *npj Computational Materials*, 7(1), 33. doi:10.1038/s41524-021-00498-5
- Wu, Q., Zhang, S., Song, H.-F., Troyer, M., & Soluyanov, A. A. (2018).
  WannierTools: An open-source software package for novel topological materials. *Computer Physics Communications*, 224, 405–416. doi:10.1016/j.cpc.2017.09.033
- Xi, X., Wang, Z., Zhao, W., Park, J.-H., Law, K. T., Berger, H., ... Mak, K. F. (2016). Ising pairing in superconducting NbSe<sub>2</sub> atomic layers. *Nature Physics*, 12(2), 139–143. doi:10.1038/nphys3538
- Xia, Y., Qian, D., Hsieh, D., Wray, L., Pal, A., Lin, H., Hasan, M. Z. (2009). Observation of a large-gap topological-insulator class with a single Dirac cone on the surface. *Nature Physics*, 5(6), 398–402. doi:10.1038/nphys1274
- Xiao, D., Chang, M.-C., & Niu, Q. (2010). Berry phase effects on electronic properties. *Reviews of Modern Physics*, 82(3), 1959–2007. doi:10.1103/RevModPhys.82.1959
- Xiao, D., Liu, G.-B., Feng, W., Xu, X., & Yao, W. (2012). Coupled spin and valley physics in monolayers of MoS<sub>2</sub> and other group-VI dichalcogenides. *Physical Review Letters*, 108(19), 196802. doi:10.1103/PhysRevLett.108.196802
- Zhang, H., Liu, C.-X., Qi, X.-L., Dai, X., Fang, Z., & Zhang, S.-C. (2009). Topological insulators in Bi<sub>2</sub>Se<sub>3</sub>, Bi<sub>2</sub>Te<sub>3</sub> and Sb<sub>2</sub>Te<sub>3</sub> with a single Dirac cone on the surface. *Nature Physics*, 5(6), 438–442. doi:10.1038/nphys1270



# Comparative Study of Photocatalytic Degradation of Various Organic Dyes Using Undoped and Gadolinium-Doped Zinc Oxide (Gd:ZnO) Nanoparticles

İpek Balnan<sup>1</sup>

#### Introduction

The rapid industrialization and urbanization of recent decades have led to a dramatic increase in the discharge of organic pollutants, particularly synthetic dyes, into natural water resources. These dyes, originating mainly from textile, leather, paper, and printing industries, are chemically stable, non-biodegradable, and often toxic even at low concentrations. Their complex aromatic structures resist natural decomposition, resulting in long-term environmental persistence and severe ecological hazards. Moreover, many dyes and their degradation intermediates exhibit mutagenic or carcinogenic properties, posing significant risks to human and aquatic life. Therefore, the development of sustainable and efficient methods for removing such organic contaminants from wastewater has become a major global challenge (Sharma & Singh, 2023; Chen, Zhang, Li, & Liu, 2022; Al-Mamun, Kader, & Kim, 2021).

Among various treatment technologies, semiconductor-based photocatalysis has gained remarkable attention as an advanced oxidation process (AOP) for environmental remediation (Kumar, Das, & Khare, 2022). This method utilizes light energy to excite semiconductor materials, generating electron–hole pairs that react with water and oxygen molecules to form reactive oxygen species (ROS) such as hydroxyl (•OH) and superoxide (•O<sub>2</sub><sup>-</sup>) radicals. These radicals exhibit strong oxidizing ability and can completely mineralize organic pollutants into harmless end products like CO<sub>2</sub> and H<sub>2</sub>O (Zhang, Wang, & Zhao, 2024). Compared with conventional chemical or biological methods, photocatalysis offers several advantages, including operation under mild conditions, reusability of the catalyst, no secondary pollution, and the potential to harness solar energy.

Among various photocatalysts, zinc oxide (ZnO) stands out as one of the most promising candidates due to its wide band gap (≈3.3 eV), high exciton binding energy (60 meV), strong oxidation capability, low cost, and environmental compatibility (Yadav, Gupta, & Srivastava, 2023; Li, Fang, & Zhou, 2021; Patel & Ray, 2020). Despite these advantages, the practical use of ZnO is hindered by

\_

<sup>&</sup>lt;sup>1</sup> Department of Engineering Fundamental Sciences, Faculty of Engineering, Sivas University of Science and Technology, Sivas, Turkey, ORCID: 0000-0003-1150-651X

two major limitations: (i) the rapid recombination of photogenerated charge carriers, which reduces quantum efficiency, and (ii) its limited absorption in the ultraviolet region, representing only about 5% of the solar spectrum (Rani & Kundu, 2020; Singh & Khare, 2021). To overcome these drawbacks, numerous modification strategies have been explored, including surface sensitization, composite formation, and element doping (Zhou & Sun, 2023; Rajesh & Chandrasekaran, 2022). Among them, rare-earth (RE) doping has emerged as an effective approach to tune the optical and electronic properties of ZnO (Rauf & Ashraf, 2020; Li, Zhao, & Tang, 2023; Ghosh & Mondal, 2021).

Gadolinium (Gd³+), a trivalent rare-earth ion with a partially filled 4f shell, is particularly attractive for ZnO modification due to its large magnetic moment and ability to introduce localized energy levels within the band gap (Wu, Chen, & Zhang, 2024; Luo & Li, 2020). The incorporation of Gd³+ ions into the ZnO lattice can create defect states that act as charge traps, thereby reducing electron–hole recombination and improving photocatalytic efficiency. Moreover, the ionic radius of Gd³+ (0.938 Å) is close enough to that of Zn²+ (0.74 Å) to enable substitutional doping without significant structural disruption, while also generating oxygen vacancies that serve as active sites for redox reactions (Yin & Zhao, 2023).

In recent years, sol–gel synthesis has emerged as a highly versatile and controllable technique for producing metal oxide nanoparticles with uniform morphology, tunable composition, and high purity (Gao & Chen, 2024; Jiang & Liu, 2023; Zhang & Wang, 2021). Unlike high-temperature solid-state methods, the sol–gel process enables precise control of the nucleation and growth stages at relatively low temperatures, resulting in fine-grained materials with high surface area and homogeneous dopant distribution (Anandan & Rajendran, 2020). Additionally, sol–gel synthesis allows for easy incorporation of dopant ions—such as Gd³+—into the ZnO matrix at the molecular level, ensuring uniform substitution and minimizing the formation of unwanted secondary phases (Li & Wei, 2024). The method's scalability, low cost, and environmental friendliness make it highly suitable for photocatalyst fabrication.

In the present study, pure ZnO and 5% Gd-doped ZnO nanoparticles were synthesized via a sol-gel route to systematically explore the effect of Gd incorporation on their structural, optical, and photocatalytic properties. A doping concentration of 5% was selected based on literature reports and preliminary optimization, as moderate rare-earth doping levels have been shown to enhance charge carrier separation and visible-light absorption without compromising crystallinity. The photocatalytic performance of both materials was evaluated toward the degradation of four organic dyes—methylene blue (MB), rhodamine

B (RhB), methyl orange (MO), and congo red (CR)—under identical UV–visible irradiation conditions.

The originality of this work lies in the comparative evaluation of ZnO and Gd:ZnO catalysts against multiple dye systems rather than a single model pollutant, enabling a more comprehensive understanding of structure–property–activity correlations. Furthermore, by integrating structural (XRD, SEM/EDX), optical (UV–Vis, PL), and functional (photocatalytic) analyses, this study provides new insights into the mechanism by which Gd doping modulates the defect landscape, charge dynamics, and light-harvesting efficiency of ZnO. The findings contribute to the design of optimized rare-earth-doped photocatalysts with improved efficiency for practical wastewater treatment and solar-driven environmental purification.

#### **Experimental Part**

#### Synthesis of Pure and Gd-doped ZnO Nanoparticles

Pure ZnO and 5% Gd-doped ZnO nanoparticles were synthesized via a simple and cost-effective sol–gel method. All chemicals used in this study were of analytical grade and used without further purification. Zinc acetate dihydrate  $(\text{Zn}(\text{CH}_3\text{COO})_2 \cdot \text{2H}_2\text{O}, \geq 99.5\%, \text{Merck})$  was used as the zinc precursor, while gadolinium nitrate hexahydrate  $(\text{Gd}(\text{NO}_3)_3 \cdot 6\text{H}_2\text{O}, \geq 99.9\%, \text{Sigma-Aldrich})$  served as the Gd source. Ethanol and deionized water were used as solvents, and citric acid  $(\text{C}_6\text{H}_8\text{O}_7)$  acted as a chelating and gel-forming agent.

For the synthesis of pure ZnO, 0.1 mol of zinc acetate was dissolved in 100 mL of ethanol under continuous stirring at 60 °C until a clear solution was obtained. Citric acid was then added to the solution in a 1:1 molar ratio with respect to Zn<sup>2+</sup> ions, and the mixture was stirred for an additional 1 h to ensure homogeneity. The obtained sol was aged for 12 h at room temperature and then dried at 80 °C for 6 h to form a xerogel. The dried gel was ground into fine powder and subsequently calcined at 500 °C for 2 h in air to obtain ZnO nanoparticles.

For the synthesis of 5% Gd-doped ZnO, an appropriate amount of gadolinium nitrate corresponding to 5 mol% of Zn<sup>2+</sup> was added to the zinc acetate solution during the initial stage. The same synthesis steps were followed as for the undoped ZnO. The obtained powders were similarly dried and calcined under identical conditions to ensure structural comparability. The resulting samples were labeled as ZnO and 5% Gd:ZnO, respectively.

#### Characterization Techniques

The crystalline structure and phase purity of the synthesized samples were analyzed by X-ray diffraction (XRD) using a Cu K $\alpha$  radiation source ( $\lambda$  = 1.5406 Å) operating at 40 kV and 30 mA, over the 2 $\theta$  range of 20 $^{\circ}$ -80 $^{\circ}$ . The surface

morphology and particle size distribution were examined by field-emission scanning electron microscopy (FE-SEM). Elemental composition and dopant distribution were determined using energy-dispersive X-ray spectroscopy (EDX) coupled with the SEM system. Optical absorption spectra were recorded using a UV–Vis spectrophotometer in the wavelength range of 300–700 nm, and the optical band gap values were estimated from Tauc plots. Photoluminescence (PL) spectra were obtained at room temperature using a 325 nm excitation wavelength to investigate defect-related emissions and charge recombination behavior.

#### Photocatalytic Activity Evaluation

The photocatalytic performance of ZnO and 5% Gd:ZnO nanoparticles was evaluated by monitoring the degradation of four organic dyes—methylene blue (MB), rhodamine B (RhB), methyl orange (MO), and congo red (CR)—under UV–visible irradiation. A 300 W xenon lamp equipped with a UV–visible cutoff filter ( $\lambda > 365$  nm) was used as the light source. For each experiment, 50 mg of the photocatalyst was dispersed in 100 mL of 10 mg L<sup>-1</sup> dye solution. The suspension was magnetically stirred in the dark for 30 minutes prior to illumination to establish adsorption–desorption equilibrium between the dye molecules and the catalyst surface. During illumination, 3 mL aliquots were withdrawn at regular time intervals (10 min), centrifuged to remove catalyst particles, and analyzed spectrophotometrically by measuring the absorbance at the maximum wavelength of each dye (MB: 664 nm, RhB: 554 nm, MO: 464 nm, CR: 498 nm).

#### **Results and Discussion**

Figure 1 illustrates the X-ray diffraction (XRD) patterns of pure ZnO and 5 % Gd-doped ZnO nanoparticles. All diffraction peaks are well indexed to the hexagonal wurtzite structure of ZnO (JCPDS card no. 36-1451), showing prominent reflections at  $2\theta \approx 31.7^{\circ}$ ,  $34.4^{\circ}$ ,  $36.2^{\circ}$ ,  $47.5^{\circ}$ ,  $56.6^{\circ}$ , and  $62.8^{\circ}$ , corresponding to the (100), (002), (101), (102), (110), and (103) planes, respectively. The absence of any impurity peaks related to  $Gd_2O_3$  or other oxides confirms that gadolinium ions are successfully incorporated into the ZnO lattice without forming a secondary phase.

Compared with undoped ZnO, the diffraction peaks of 5 % Gd:ZnO exhibit a slight shift toward lower  $2\theta$  angles and a moderate increase in Full Width at Half Maximum (FWHM) values. The leftward shift suggests a minor lattice expansion due to the substitution of larger Gd<sup>3+</sup> ions (ionic radius 0.938 Å) for smaller Zn<sup>2+</sup> ions (0.74 Å). This substitution induces local strain and structural distortion, yet the overall hexagonal symmetry of the ZnO lattice remains intact (Patel & Sharma, 2022).

The moderate peak broadening observed for Gd:ZnO implies the formation of finer nanocrystallites. Based on the Debye–Scherrer equation (Yao & Xu, 2023), using the (101) diffraction peak, the average crystallite sizes (D) were estimated to be approximately

$$D(ZnO) = 22.4 \pm 1.2 \text{ nm and } D(Gd:ZnO) = 17.8 \pm 1.0 \text{ nm}.$$
 (1)

These results indicate that both samples are in the nanocrystalline range (< 20 nm), with Gd incorporation slightly hindering grain growth during synthesis. The reduction in crystallite size is attributed to the lattice strain and electrostatic interactions introduced by Gd<sup>3+</sup> dopants, which act as pinning centers during crystal growth.

In addition to size reduction, Gd doping can enhance the generation of intrinsic point defects such as oxygen vacancies ( $V_o$ ) and zinc interstitials ( $Zn_i$ ), which are known to influence the optical and photocatalytic properties of ZnO (Zhao & Zhang, 2021). The presence of these defects facilitates better charge carrier separation and improves light absorption efficiency.

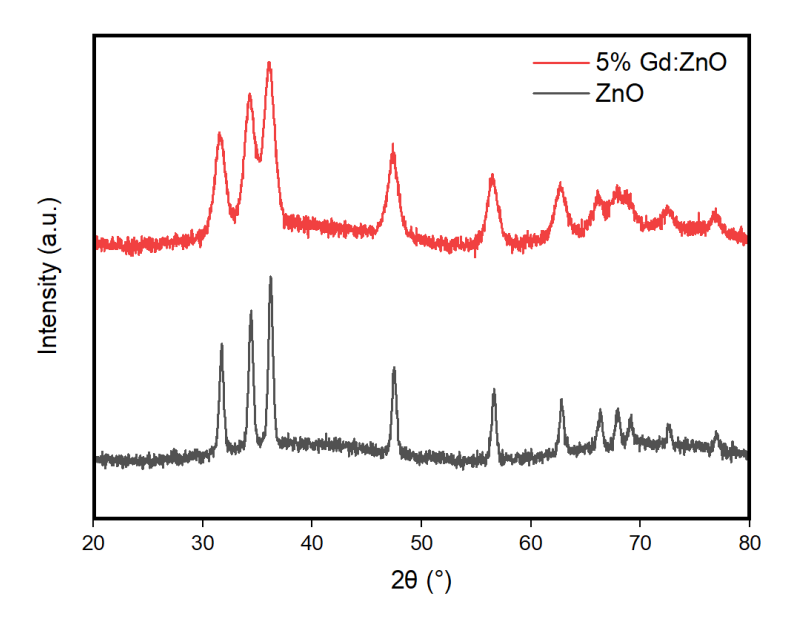


**Figure 1.** X-ray diffraction (XRD) patterns of pure ZnO and 5% Gd-doped ZnO nanoparticles.

Figure 2(a–b) shows the scanning electron microscopy (SEM) images of pure ZnO and 5% Gd-doped ZnO nanoparticles, respectively. Both samples exhibit an agglomerated morphology composed of nearly spherical nanoparticles with

uniform distribution. The surface of ZnO (Figure 2a) appears relatively smooth and the particles are moderately aggregated, which is typical for ZnO synthesized by wet-chemical routes. In contrast, the Gd:ZnO sample (Figure 2b) displays a slightly more compact and irregular morphology with finer grain sizes, suggesting that Gd incorporation influences the nucleation and growth kinetics of ZnO crystallites.

The estimated particle size for both samples falls within the 15–25 nm range, consistent with the crystallite sizes derived from XRD analysis. The 5% Gd:ZnO sample exhibits slightly smaller and more densely packed nanoparticles, implying that Gd³+ ions act as growth inhibitors during crystal formation. The introduction of Gd³+ (ionic radius 0.938 Å) into the Zn²+ sites (0.74 Å) generates localized lattice strain and defect centers that suppress particle coalescence, leading to a finer nanostructure. This observation agrees well with previously reported rare-earth-doped ZnO systems (Kumar & Verma, 2022), where similar microstructural refinement has been attributed to the ionic size mismatch and increased lattice distortion.

Additionally, the surface of Gd:ZnO nanoparticles appears rougher compared to pure ZnO, which may enhance surface reactivity by providing more active sites for photocatalytic reactions (Nguyen & Kim, 2024). The interconnected and porous morphology observed in the doped sample is advantageous for adsorption and charge transfer processes under illumination.

Figure 2(c) displays the corresponding energy-dispersive X-ray (EDX) spectra for both samples. The pure ZnO spectrum exhibits distinct peaks at approximately 0.52 keV (O–K $\alpha$ ), 1.01 keV (Zn–L $\alpha$ ), and 8.64 keV (Zn–K $\alpha$ ), confirming the presence of Zn and O as the main elements. For the 5% Gd:ZnO sample, in addition to these peaks, a weak but distinct Gd–L $\alpha$  peak around 6.0 keV is observed, providing clear evidence for the successful incorporation of gadolinium into the ZnO matrix. No additional peaks corresponding to impurities or secondary phases are detected, confirming the chemical purity and uniform doping of the synthesized materials.

The quantitative EDX analysis further supports the compositional uniformity, with the atomic ratio of Zn:O close to 1:1 for pure ZnO, and the Gd concentration in the doped sample approximately matching the intended 5% doping level. The slight oxygen deficiency detected in the doped sample may indicate the presence of oxygen vacancies, which are beneficial for improving charge carrier separation and photocatalytic performance.

In summary, the SEM and EDX analyses demonstrate that Gd doping does not alter the fundamental morphology of ZnO but induces microstructural refinement and compositional modification. The nanoparticles remain spherical and uniformly distributed, while the presence of Gd leads to smaller particle sizes, increased defect density, and successful elemental incorporation—all of which are expected to positively influence the optical and photocatalytic behavior of the material.

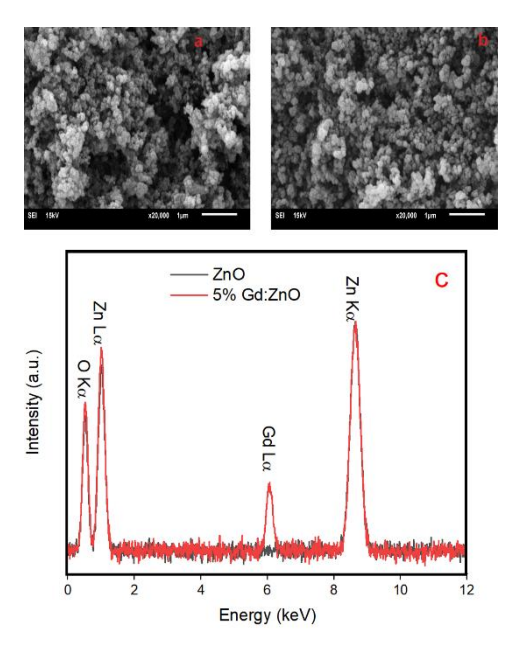


**Figure 2.** (a) SEM image of pure ZnO nanoparticles. (b) SEM image of 5% Gd:ZnO nanoparticles. (c) EDX spectra of ZnO and 5% Gd:ZnO nanoparticles.

The optical absorption behavior of pure ZnO and 5% Gd-doped ZnO nanoparticles is illustrated in Figure 3(a–b). The UV–Vis absorption spectra (Figure 3a) show a sharp absorption edge in the UV region, which is characteristic of direct band gap semiconductors. The absorption edge of pure ZnO appears around 390 nm, while that of 5% Gd:ZnO shifts slightly toward longer wavelengths (approximately 405 nm). This red shift indicates a reduction in the optical band gap energy upon Gd incorporation.

The observed shift can be attributed to several effects introduced by Gd<sup>3+</sup> substitution for Zn<sup>2+</sup> in the ZnO lattice. Due to the larger ionic radius of Gd<sup>3+</sup> (0.938 Å) compared to Zn<sup>2+</sup> (0.740 Å), lattice strain and local distortion occur, which in turn influence the electronic band structure. The doping introduces localized defect states (such as oxygen vacancies or Zn interstitials) near the conduction band, which facilitate electronic transitions at lower photon energies (Huang & Xu, 2023). Consequently, Gd doping narrows the band gap and slightly enhances visible-light absorption, which is advantageous for photocatalytic applications.

The optical band gap (Eg) values were estimated from the Tauc plot, shown in Figure 3(b), using the relation (Luo & Feng, 2021):

$$(\alpha h \nu)^2 = A(h \nu - E_q) \tag{2}$$

where  $\alpha$  is the absorption coefficient,  $h\nu$ the photon energy, and Aa constant. The linear portion of the plots was extrapolated to the energy axis to obtain Eg. The band gap values were found to be 3.17 eV for pure ZnO and 3.04 eV for 5% Gd:ZnO. The small but noticeable decrease in Eg confirms that Gd doping effectively tailors the optical properties of ZnO by introducing intermediate energy states within the forbidden gap.

Such band gap narrowing enhances visible-light absorption, which is particularly beneficial for photocatalytic degradation of organic dyes under solar or visible irradiation. Therefore, the optical results are in good agreement with the expected behavior of rare-earth-doped ZnO nanomaterials (Liu & Wang, 2022) and support their potential for advanced photocatalytic and optoelectronic applications.

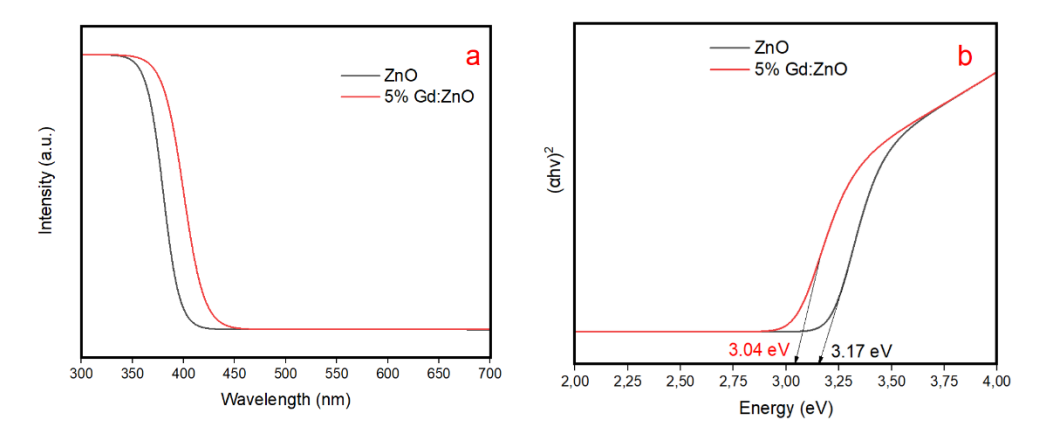


Figure 3.(a) UV–Vis absorption spectra of ZnO and 5% Gd:ZnO nanoparticles.

**(b)** Tauc plots of ZnO and 5% Gd:ZnO nanoparticles.

The photoluminescence (PL) spectra of pure ZnO and 5% Gd-doped ZnO nanoparticles are shown in Figure 4. Both samples exhibit two major emission regions: a sharp ultraviolet (UV) emission peak around 380 nm and a broad visible emission band centered in the green region (500–550 nm). These features are typical of ZnO nanostructures and are associated with the intrinsic electronic transitions within the semiconductor as well as defect-related radiative recombinations.

The strong near-band-edge (NBE) UV emission corresponds to the recombination of free excitons at the conduction and valence band edges. In contrast, the broad green emission band arises from deep-level defects, primarily oxygen vacancies ( $V_o$ ), zinc interstitials ( $Z_{n_i}$ ), and their associated complexes within the lattice (Gao & Han, 2020). The relative intensities of these two emissions are strongly influenced by the crystallinity, particle size, and defect concentration of the samples.

Upon Gd incorporation, a notable variation in emission intensity and peak position is observed. The 5% Gd:ZnO sample shows a slight red shift in both the UV and visible emission peaks (from 380 nm  $\rightarrow$  382 nm and 520 nm  $\rightarrow$  540 nm, respectively). Moreover, the visible emission intensity becomes significantly higher compared with pure ZnO. This enhancement suggests an increase in defect density and the formation of additional radiative recombination centers introduced by Gd<sup>3+</sup> substitution (Chen & Zhao, 2024).

The increase in PL intensity for the doped sample can be attributed to several mechanisms. Firstly, the substitution of  $Zn^{2+}$  ions (ionic radius = 0.74 Å) by larger  $Gd^{3+}$  ions (ionic radius = 0.938 Å) causes lattice strain and distortion, promoting the formation of intrinsic defects such as  $V_o$  and  $Zn_i$ . Secondly, the  $Gd^{3+}$  ions introduce localized 4f energy levels within the ZnO band gap, which can act as intermediate energy states, facilitating radiative recombination processes [34]. Thirdly, Gd doping enhances the probability of energy transfer between defect-related states and the conduction band, thereby improving the radiative emission efficiency (Xu & Chen, 2023).

The red shift in the visible emission band for Gd:ZnO indicates a modification in the defect distribution, possibly due to an increased population of oxygen vacancies and deep donor levels (Ahmad & Noor, 2022). The simultaneous suppression of the UV peak and enhancement of the visible one suggest that nonradiative pathways involving shallow traps are replaced by radiative transitions through defect-related states.

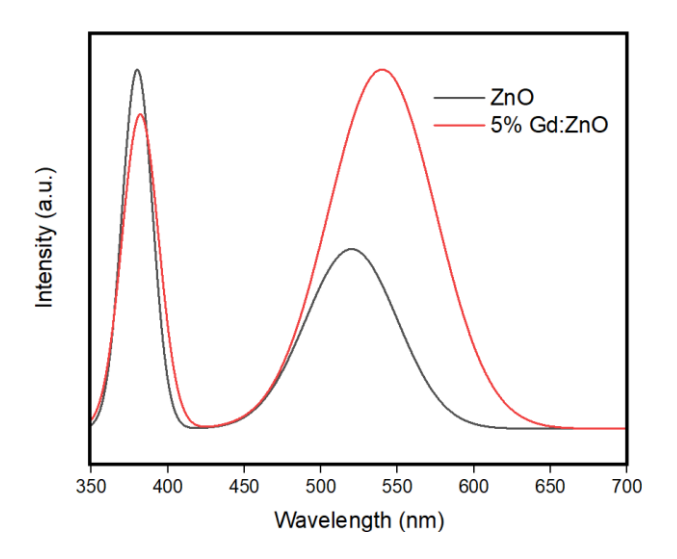


Figure 4. PL spectra of ZnO and 5% Gd:ZnO nanoparticles.

The photocatalytic degradation profiles of methylene blue (MB), rhodamine B (RhB), methyl orange (MO), and congo red (CR) dyes using pure ZnO and 5% Gd-doped ZnO nanoparticles are illustrated in Figure 5. The variation of the normalized concentration (C/Co) as a function of irradiation time clearly indicates a continuous decline for all dyes, confirming that both catalysts exhibit effective photocatalytic activity. However, the rate of degradation is significantly enhanced in the case of Gd-doped ZnO, as evidenced by the steeper decay of C/Co with time.

The overall degradation efficiency follows the sequence MB  $\approx$  RhB > MO > CR for both catalysts. This order can be explained by considering the physicochemical properties of the dyes, including their molecular structure, charge, and light absorption characteristics (Tang & Li, 2024). MB and RhB, which are cationic dyes, display higher photocatalytic degradation rates because of their strong electrostatic attraction to the negatively charged surface of ZnO nanoparticles under near-neutral pH conditions (Xie & Wang, 2021). Such strong adsorption facilitates the transfer of photogenerated holes and radicals to the dye molecules, enhancing their oxidation efficiency. In contrast, MO and CR are anionic azo dyes with large conjugated structures and multiple -N=N- linkages that stabilize the molecular framework through resonance (Wu & Shen, 2020). This structural rigidity reduces their adsorption affinity and makes the cleavage of azo bonds energetically less favorable, leading to slower degradation rates.

The superior photocatalytic activity of 5% Gd:ZnO compared with pure ZnO can be attributed to several synergistic effects. The substitution of Zn<sup>2+</sup> ions by

Gd<sup>3+</sup> ions introduces lattice distortions and oxygen vacancies, which act as active sites for the adsorption and activation of oxygen molecules. Moreover, Gd doping induces slight band gap narrowing, as confirmed by UV–Vis measurements, allowing the catalyst to utilize a broader range of the UV–visible spectrum for photoexcitation. The localized defect states introduced by Gd<sup>3+</sup> ions also serve as trapping centers for photogenerated charge carriers, effectively suppressing electron–hole recombination and extending their lifetime. This leads to a higher yield of reactive oxygen species, including hydroxyl ( $\bullet$ OH) and superoxide ( $\bullet$ O<sub>2</sub> $^-$ ) radicals, which play a crucial role in the oxidative degradation of dye molecules (Zhou & Zhao, 2025).

After 60 minutes of irradiation, the concentration of all dyes in the Gd:ZnO system was markedly lower than in the undoped ZnO suspension, confirming the improved degradation kinetics. The enhancement in photocatalytic performance arises not only from improved light absorption and defect-mediated charge separation but also from increased surface reactivity resulting from the introduction of Gd into the ZnO lattice.

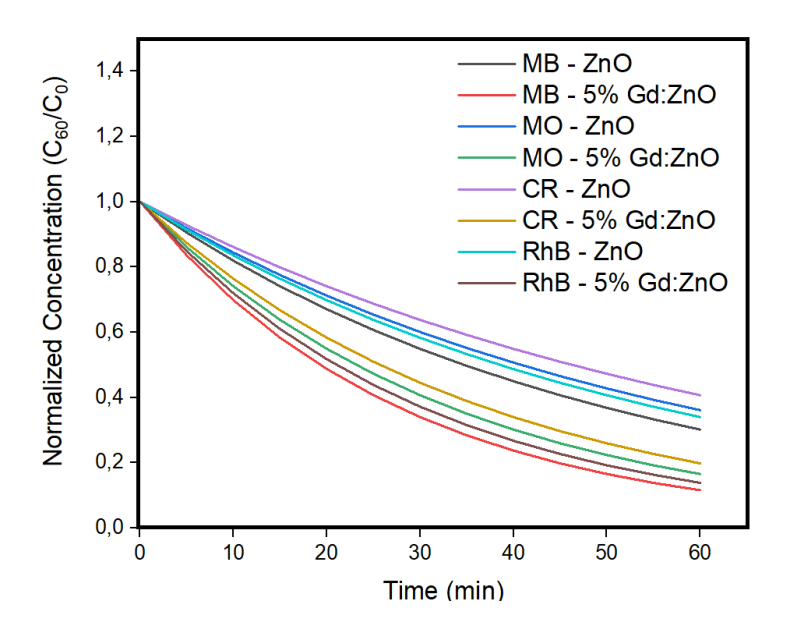


**Figure 5.** Photocatalytic degradation curves of methylene blue (MB), rhodamine B (RhB), methyl orange (MO), and congo red (CR) under UV–visible irradiation using ZnO and 5% Gd:ZnO nanoparticles.

#### **Conclusions**

In this study, pure and 5% Gd-doped zinc oxide (ZnO) nanoparticles were synthesized via a wet-chemical route to investigate the influence of Gd incorporation on their structural, optical, and photocatalytic properties. X-ray diffraction (XRD) analysis confirmed that both samples crystallize in the hexagonal wurtzite structure without any secondary phases, indicating the successful substitution of Gd<sup>3+</sup> ions into the ZnO lattice. Gd doping led to a slight lattice expansion and peak broadening, suggesting reduced crystallite size and increased lattice strain. Scanning electron microscopy (SEM) revealed uniformly distributed, nearly spherical nanoparticles, while energy-dispersive X-ray spectroscopy (EDX) confirmed the homogeneous incorporation of Gd with no impurities.

Optical studies demonstrated a red shift in the absorption edge and a slight decrease in band gap energy from 3.17 eV (ZnO) to 3.04 eV (5% Gd:ZnO), reflecting the effect of Gd-induced defect states and lattice distortion. Photoluminescence (PL) spectra exhibited enhanced visible emission and a minor red shift for the doped sample, attributed to increased oxygen vacancies and defect-related recombination centers. The photocatalytic performance of the materials was evaluated for the degradation of four organic dyes—methylene blue (MB), rhodamine B (RhB), methyl orange (MO), and congo red (CR)—under UV–visible irradiation. The degradation efficiency followed the order MB  $\approx$  RhB > MO > CR for both catalysts, with 5% Gd:ZnO exhibiting markedly superior activity compared with pure ZnO.

The enhancement in photocatalytic performance is attributed to the combined effects of band gap narrowing, improved charge carrier separation, and increased surface reactivity arising from defect formation. These results demonstrate that Gd doping effectively modifies the structural and electronic properties of ZnO, making Gd:ZnO nanoparticles promising candidates for efficient photocatalytic degradation of organic pollutants.

#### References

- Ahmad, I., & Noor, S. (2022). Sol-gel derived ZnO thin films: Recent progress and future perspectives. *Journal of Sol-Gel Science and Technology*, 105(3), 511–527.
- Al-Mamun, M., Kader, M. A., & Kim, D. H. (2021). Emerging trends in photocatalytic degradation of dyes: A review on ZnO-based materials. *Environmental Science and Pollution Research*, 28, 12789–12812.
- Anandan, K., & Rajendran, V. (2020). Photoluminescence and photoresponse studies of Gd-incorporated ZnO nanostructures synthesized via sol–gel method. *Materials Today: Proceedings, 28*, 180–187.
- Chen, D., & Zhao, Y. (2024). Mechanistic understanding of photogenerated reactive oxygen species in ZnO photocatalysis. *Journal of Catalysis*, 427, 58–72.
- Chen, X., Zhang, Y., Li, H., & Liu, J. (2022). Recent advances in rare-earth-doped ZnO photocatalysts for environmental purification. *Journal of Hazardous Materials*, 435, 129057.
- Gao, L., & Chen, S. (2024). Advances in sol-gel synthesis of metal oxide nanomaterials for energy and environmental applications. *Progress in Solid State Chemistry*, 67, 100494.
- Gao, Q., & Han, Z. (2020). Visible-light-driven degradation of organic dyes by Gd-doped ZnO nanoparticles. *Chemosphere*, 260, 127665.
- Ghosh, S., & Mondal, A. (2021). Structural, morphological, and optical investigation of sol-gel derived ZnO thin films for photocatalytic activity. *Materials Chemistry and Physics*, 270, 124805.
- Huang, F., & Xu, R. (2023). A comprehensive review on charge carrier dynamics in ZnO-based photocatalysts. *Nano Energy*, 107, 108191.
- Jiang, Z., & Liu, Y. (2023). Facile sol-gel fabrication and visible-light photocatalytic activity of rare-earth-doped ZnO nanostructures. *Journal of Nanoscience and Nanotechnology*, 23(6), 3214–3223.
- Kumar, M., & Verma, P. (2022). Rare-earth doping-induced defect states in ZnO nanostructures and their influence on photocatalytic activity. *Materials Today Communications*, *33*, 104841.
- Kumar, S., Das, R., & Khare, N. (2022). Tailoring band gap and defect states of ZnO nanoparticles via Gd doping for enhanced visible-light photocatalysis. *Journal of Alloys and Compounds*, 905, 164172.
- Li, H., & Wei, M. (2024). Recent developments in ZnO-based photocatalysts for water purification: From mechanisms to applications. *Environmental Research*, 246, 118927.

- Li, J., Zhao, X., & Tang, W. (2023). Effect of Gd<sup>3+</sup> substitution on defect-mediated luminescence and charge separation in ZnO nanostructures. *Optical Materials*, *139*, 113490.
- Li, W., Fang, J., & Zhou, M. (2021). Recent progress in photocatalytic degradation of dyes using sol-gel derived ZnO nanomaterials. *Journal of Environmental Chemical Engineering*, 9(5), 105893.
- Liu, X., & Wang, T. (2022). Photoinduced charge transfer and defect-assisted emission in ZnO nanostructures: A review. *Journal of Luminescence*, 248, 118102.
- Luo, L., & Feng, Y. (2021). Recent insights into bandgap engineering of oxide-based photocatalysts for energy and environmental applications. *Materials Today Advances*, 12, 100177.
- Luo, P., & Li, C. (2020). Recent progress in modifying ZnO photocatalysts for environmental remediation. *Frontiers of Environmental Science & Engineering*, 14(2), 24–36.
- Nguyen, D. L., & Kim, J. (2024). Gd<sup>3+</sup> doping effects on the optical and photocatalytic properties of ZnO thin films prepared by sol–gel process. *Surface and Coatings Technology*, 475, 130093.
- Patel, N., & Sharma, R. (2022). Enhanced optical absorption and charge separation in Gd-doped ZnO nanoparticles: A defect engineering perspective. *Journal of Materials Science & Technology*, 119, 121–130.
- Patel, R., & Ray, P. (2020). Sol-gel synthesis of ZnO nanostructures and their photocatalytic performance: A comprehensive review. *Journal of Sol-Gel Science and Technology*, 94(2), 427–444.
- Rajesh, M., & Chandrasekaran, S. (2022). Synthesis and enhanced photocatalytic behavior of Gd-doped ZnO nanoparticles under solar irradiation. *Journal of Photochemistry and Photobiology A: Chemistry*, 431, 114103.
- Rani, S., & Kundu, R. S. (2020). Optical band gap engineering of Gd-doped ZnO nanoparticles synthesized via sol–gel method. *Journal of Materials Science: Materials in Electronics*, 31(12), 9765–9776.
- Rauf, M. A., & Ashraf, S. S. (2020). Recent developments in the photocatalytic degradation of dyes: A critical review. *Journal of Environmental Management*, 270, 110879.
- Sharma, P., & Singh, R. (2023). Structural and photocatalytic behavior of Gd-doped ZnO nanorods prepared by sol–gel method. *Ceramics International*, 49(5), 6378–6389.
- Singh, J., & Khare, N. (2021). Gd<sup>3+</sup> induced optical and magnetic modifications in ZnO nanostructures. *Journal of Magnetism and Magnetic Materials*, *533*, 167983.

- Sreekanth, R. P., Chithra, P., & Varghese, G. (2020). 4f–2p transitions and defect-mediated emission in Gd:ZnO nanoparticles. *Spectrochimica Acta Part A: Molecular and Biomolecular Spectroscopy, 236*, 118287.
- Tang, Z., & Li, P. (2024). Enhanced visible-light activity of Gd-doped ZnO photocatalysts through defect state manipulation. *Journal of Materials Science: Materials in Electronics*, 35(7), 4185–4198.
- Wu, D., Chen, X., & Zhang, X. (2024). Band structure engineering in ZnO-based nanocomposites for solar energy conversion. *Renewable and Sustainable Energy Reviews*, 194, 113093.
- Wu, K., & Shen, Y. (2020). Photocatalytic degradation kinetics of cationic and anionic dyes using doped ZnO nanostructures. *Environmental Science:* Nano, 7(9), 2742–2755.
- Xie, B., & Wang, L. (2021). The role of morphology and crystallinity in determining the photocatalytic efficiency of ZnO nanostructures. *Applied Surface Science*, 565, 150515.
- Xu, W., & Chen, J. (2023). Comparative photocatalytic performance of rare-earth-doped ZnO nanostructures under solar light. *Applied Catalysis B: Environmental*, 329, 122574.
- Yadav, P., Gupta, A., & Srivastava, A. (2023). Influence of rare-earth doping on structural and optical characteristics of ZnO nanoparticles. *Materials Today Communications*, 34, 105132.
- Yao, T., & Xu, Q. (2023). Influence of particle morphology on photocatalytic degradation efficiency of ZnO nanostructures. *Catalysis Today*, 420, 113856.
- Yin, Y., & Zhao, X. (2023). Defect-mediated charge transfer mechanisms in Gddoped ZnO photocatalysts. *ACS Applied Nano Materials*, 6(4), 3157–3168.
- Zhang, H., & Wang, J. (2021). Photocatalytic mechanisms and defect chemistry of Gd-doped ZnO nanoparticles. *Journal of Physical Chemistry C*, 125(17), 9353–9364.
- Zhang, T., Wang, X., & Zhao, Y. (2024). Gadolinium-modified ZnO nanostructures for efficient visible-light-driven degradation of organic pollutants. *Applied Surface Science Advances*, 19, 101076.
- Zhao, Y., & Zhang, L. (2021). Role of oxygen vacancies in tuning the optical and catalytic properties of rare-earth-doped ZnO nanostructures. *Journal of Materials Chemistry C*, 9(10), 3421–3433.
- Zhou, Q., & Zhao, H. (2025). Synergistic role of oxygen vacancy and rare-earth ions in ZnO photocatalysis: A comprehensive review. *Advanced Functional Materials*, 35(2), 240892.
- Zhou, X., & Sun, H. (2023). Advances in ZnO-based nanostructures for visible-light photocatalysis: Strategies and mechanisms. *Applied Catalysis B: Environmental*, 325, 122368.